

# Stratified flow past a sphere at moderate Reynolds numbers

Francesco Cocetta<sup>a</sup>, Mike Gillard<sup>a</sup>, Joanna Szmelter<sup>a</sup>,  
Piotr K. Smolarkiewicz<sup>b</sup>

<sup>a</sup>*Loughborough University, Leicestershire LE11 3TU, UK*

<sup>b</sup>*National Center for Atmospheric Research, Boulder, CO, USA*

---

## Abstract

A numerical study of stably stratified flows past spheres at Reynolds numbers  $Re = 200$  and  $Re = 300$  is reported. In these flow regimes, a neutrally stratified laminar flow induces distinctly different near-wake features. However, the flow behaviour changes significantly as the stratification increases and suppresses the scale of vertical displacements of fluid parcels. Computations for a range of Froude numbers  $Fr \in [0.1, \infty]$  show that as Froude number decreases, the flow patterns for both Reynolds numbers become similar. The representative simulations of the lee-wave instability at  $Fr = 0.625$  and the two-dimensional vortex shedding at  $Fr = 0.25$  regimes are illustrated for flows past single and tandem spheres, thereby providing further insight into the dynamics of stratified flows past bluff bodies. In particular, the reported study examines the relative influence of viscosity and stratification on the dividing streamline elevation, wake structure and flow separation. The solutions of the Navier-Stokes equations in the incompressible Boussinesq limit are obtained on unstructured meshes suitable for simulations involving multiple bodies. Computations are accomplished using the finite volume, non-oscillatory forward-in-time (NFT) Multidimensional Positive Definite Transport Algorithm (MPDATA) based solver. The impact and validity of the numerical approximations, especially for the cases exhibiting strong stratification, are also discussed. Qualitative and quantitative comparisons with available laboratory experiments and prior numerical studies confirm the validity of the numerical approach.

*Key words:* stably stratified flows, flows past a sphere, incompressible viscous flows, unsteady internal waves

---

\* Corresponding Author.

*Email address:* j.szmelter@lboro.ac.uk (Joanna Szmelter).

## 1 Introduction

Stably stratified flows past a sphere display an array of intricate physical phenomena epitomising flow responses to localised three-dimensional obstacles. The benchmark emulating a spherical body moving through a stratified fluid provides a convenient framework for investigating both the flow behaviour and the numerical methods employed to simulate flows at a range of Reynolds and Froude numbers. Viscous stratified flows have important applications in diverse areas of engineering and geoscience, where examples include wind turbines and marine appliances submersed in thermoclines [9], flows of ocean currents past natural bathymetry [56] as well as atmospheric flows past mountains and islands [21,34]. Such practical interests motivate numerical simulations complementing idealised experimental studies of flows past a sphere. However, despite a large body of experimental and numerical work devoted to stratified wakes behind spheres, the numerical simulations actually resolving the viscous boundary layer past a sphere are rare due to their technical complexity; see [54,30] for recent succinct reviews.

Experimental studies, e.g. [26,15,23,3], demonstrate the importance of the relative ratio of the characteristic time scales of the viscous and buoyant forces to the time scale of inertia. These studies suggest that the structure of a flow depends largely on the fluid stratification and its interaction with viscous effects—characterised, respectively, by the Froude  $Fr = V_o/Nh$  and Reynolds  $Re = V_oL/\nu$  numbers, with  $V_o$ ,  $N$ ,  $h$ ,  $L$ , and  $\nu$  corresponding to free stream velocity, buoyancy frequency, obstacle height, characteristic length scale, and kinematic viscosity. As  $Fr \nearrow \infty$ , weakly stratified laminar flows demonstrate three-dimensional structures reminiscent of neutrally stratified flows, whereas for  $Fr \searrow 0$  they become more planar and two-dimensional vortex shedding can be observed. The latter matches satellite observations of mesoscale eddies in the lee of mountainous islands [22]. As reported by [23,3], a range of different flow patterns occurs between the two asymptotic flow regimes. The main responses such as lee waves, obstacle-scale eddies, and upwind blocking are commonly observed in experiments. However, in terms of delimiting the transitions between the patterns, experimental data has been found to be in poor agreement [13].

The pioneering numerical study of a flow past a physical sphere towed in a linearly density-stratified incompressible fluid at  $Re = 200$  was documented by Hanazaki [14]. Hanazaki’s focus was on the spatial evolution of the near-field flow response to the sphere. Subsequent investigations spawned a range of distinct numerical strategies that were driven by diverse interests. Studies focused on temporal evolution of turbulent wakes formed behind underwater vehicles and the parameter-dependent far-field wake flow dynamics employed direct numerical simulation (DNS) [11,2,5], large eddy simulation (LES) [7],

and implicit large eddy simulation (ILES) [5]. These studies played an important role in exploring turbulent wakes and parameter-dependent flow dynamics for stratified flows. However, they either completely excluded the sphere from their simulation domains while relying on suitable initial conditions, or hybridised the spatial/temporal evolution [54]—in the spirit of secondary application models where an application of interest is driven by an output of a different model [42]. Alternative models which include a sphere immersed in the moving stratified fluid and utilise high resolution grids required to accurately represent evolution of boundary layers, separation, and the dynamics of fluids close to the sphere are computationally demanding; their application is therefore still relatively uncommon.

An explicit representation of a sphere’s geometry in a computational domain can adopt distinctly different approaches based on immersed boundaries or body-fitted meshes. Seminal DNS studies at  $Re = 3700$  [31,32] solved Navier–Stokes equations in cylindrical coordinates on a staggered grid, with a sphere represented by an immersed boundary. A broad range of stratifications were considered with  $Fr \in [1, \infty]$  [32] and  $Fr \in [0.025, 1]$  [31], respectively. These studies provided systematic investigations of buoyancy effects on the behaviour of wakes. They confirmed that buoyancy suppresses turbulence as the stratification increases, however, for low Froude numbers below approximately  $Fr = 0.25$ , a regeneration of turbulence occurs due to a new regime of vortex shedding.

Here, we adopt an alternative approach that employs unstructured meshes fitted to a sphere. It enables simulations fully resolving viscous boundary layers, important for our particular interest with quantitative drag predictions. Similar to our study, recent contributions employing body fitted meshes solved incompressible Navier Stokes equations in the Boussinesq approximation. Among them, simulations in [30] were performed for  $Fr \in [0.1, \infty]$  at  $Re = 200$  and  $Fr \in [1, \infty]$  at  $Re = 1000$ . These solutions used generalised curvilinear coordinates and were obtained on a regular non-staggered grid. A structured spherical grid conforming to the sphere was also employed in [13] with a staggered arrangement for velocity and pressure. The solutions in [13] used a hybrid finite-difference discretisation in spherical coordinates, and investigated flow regimes at  $0.005 < Fr < 100$ , for  $1 < Re < 500$ . Examples of earlier contributions utilising body fitted grids include [22], reporting simulations of flows at  $Re = 200$  and  $Fr \in [0.02, 10]$ . Their simulations were performed on a structured mesh generated in a cylindrical domain composed of brick and prismatic shaped elements with a mixed finite element discretisation for velocity and pressure. The ancestral work of Hanazaki [14] also employed a structured body fitted grid, in a study of flows at  $Re = 200$  and  $Fr \in [0.25, 200]$ . In [14] the structured grid was generated by rotating a 2D mesh created with a form of conformal mapping. Computations used cylindrical coordinates and finite difference discretisations of different orders for

pressure and velocity.

The present study builds on our earlier work [51] that documented density stratified flow calculations for  $Re = 200$  and for high Reynolds numbers in a turbulent regime appropriate for ILES. Numerical capabilities employed here extend the non-oscillatory forward-in-time finite volume (NFT-FV) approach documented in [51] through MPI parallelisation of the NFT-FV model. This extension allows for the refinement of earlier  $Re = 200$  results, in addition to investigating stratified flow past a sphere at  $Re = 300$ . Interestingly, for weak stratifications, both cases have distinctly different wake patterns: where for high Froude numbers steady state is achieved for  $Re = 200$ , whereas a characteristic structure of the hairpin vortex shedding is observed for  $Re = 300$ . However, as stratification increases the flow behaviour of the two cases starts to show strong similarities. In addition to reducing the time to solution, the parallelisation benefits the quality of simulation results. Namely, it allows for the enlargement of the computational domain that reduces the impact of the external boundaries. Moreover, it enables the refinement of the mesh resolution in proximity to the solid boundaries and in the flow wake region. Last but not least, the simulations can be run for a longer time; so flow patterns which exhibit themselves on a longer time-scale can be better detected.

Previous numerical efforts reported in the literature have been conducted exclusively on structured meshes, whereas the current implementation permits the use of more flexible unstructured meshes and overcomes the constraint of the regular grids historically adopted in simulation of stratified flows. Structured meshes (including topologically regular grids) have merits of simplicity and computational economy for homogeneous flows in simple domains. However, geophysical flows have a large degree of heterogeneity, complex geometry of bounding domains, and multiplicity of scales. In the Earth's atmosphere and oceans internal gravity waves are both ubiquitous and intricate, as their occurrence and form depend on the relative magnitude and structure of ambient flows/currents, entropy/density stratification, and forcings. The latter in particular must account for complicated variability of shorelines and topography/bathymetry. There is also an abundance of natural multiscale phenomena relevant to weather and climate for which high variation in mesh resolution is desirable. Factors limiting the flexibility of structured meshes in construction of differential operators are usually related to rigid data structures, dictated by the topological uniformity of computational cells. Furthermore, generation of body-fitted structured meshes is restricted to moderately complex geometries. For geophysical applications, terrain following coordinates are commonly used to account for orography or bathymetry. However, this approach cannot be used for shapes involving overhanging orography, underwater caves and reservoirs, or submerged objects. The generation of structured body-fitted meshes for simple geometries such as a sphere is usually accomplished via conformal mapping. The use of multiblock techniques can add some flexibility

to generate high quality structured meshes for more complex and multibody configurations, cf. [48], however, the control of the point distribution, required to capture key flow features, with conformal meshes is difficult and limited. In contrast, fully unstructured meshes adopted in this work have flexibility allowing for easy accommodation of optimal meshes and mesh adaptivity. Even more importantly, unstructured meshes allow for simulations involving arbitrary complex geometries.

For the considered flows past a sphere, unstructured meshes enable local refinement and the optimisation of mesh resolution in regions where the flow is most complex, such as the boundary layer and wake. Additionally, the capability of unstructured meshes to account for multibody configurations is demonstrated by extending our study to calculations of stratified flows past two spheres, for  $Re = 300$ , where mesh refinement in the region between the two spheres can also be used.

The remainder of the paper is organised as follows. The next section outlines the governing equations and the numerical approach employed. Section 3 documents a systematic numerical study for a range of Froude numbers  $1/Fr \in [0, 10]$  for flows past a single sphere at  $Re = 200$  and  $300$  and two spheres in a tandem configuration at  $Re = 300$ . Remarks in section 4 conclude the paper.

## 2 Numerical approach

### 2.1 Governing equations

This study is motivated by atmospheric applications, therefore the actual PDE system solved in our NFT-FV model is the Lipps-Hemler [24,25] anelastic system suitable for simulating a variety of mesoscale atmospheric flows [43,44,46]. For an ideal atmosphere, the anelastic conservation laws of mass, momentum and entropy fluctuations (1)-(3) are compactly written as

$$\nabla \cdot (\mathbf{V}\bar{\rho}) = 0 , \tag{1}$$

$$\frac{\partial \bar{\rho} V_I}{\partial t} + \nabla \cdot (\mathbf{V}\bar{\rho} \cdot V_I) = -\bar{\rho} \frac{\partial \varphi'}{\partial x_I} + \bar{\rho} g \frac{\theta'}{\theta} \delta_{I3} + (\nabla \cdot \tau)_I , \tag{2}$$

$$\frac{\partial \bar{\rho} \theta'}{\partial t} + \nabla \cdot (\mathbf{V}\bar{\rho} \theta') = -\bar{\rho} \mathbf{V} \cdot \nabla \theta_e , \tag{3}$$

where  $V_{I(=1,2,3)}$  indicate the velocity components in the  $x_I$  Cartesian coordinate directions  $(x, y, z)$ , with time  $t$ , the Kronecker delta  $\delta_{IJ}$ , and potential

temperature  $\theta$  related to specific entropy via  $ds = c_p d \ln \theta$  (with  $c_p$  denoting specific heat at constant pressure). Density and pressure are symbolised by  $\rho$  and  $p$ , while an overline and subscript “ $e$ ” mark the static reference state and a stably stratified inertial ambient state, respectively; cf. [43] for a discussion. A density normalised perturbation pressure in the momentum equation (2) is given by  $\varphi' = (p - p_e)/\bar{\rho}$ , while the gravitational acceleration  $g$  enters the buoyancy term on the RHS of (2), where  $\theta' = \theta - \theta_e$  is the potential temperature perturbation about the ambient profile  $\theta_e(x_3) = \theta_o \exp(Sx_3)$ ; hereafter stratification  $S$  is assumed constant and “ $o$ ” subscript refers to constant reference values. The deviatoric stress tensor  $\tau$  in the last term on the RHS of (2) is defined by

$$\tau_{IJ} = \mu \left( \frac{\partial V_I}{\partial x_J} + \frac{\partial V_J}{\partial x_I} \right). \quad (4)$$

where  $\mu = \bar{\rho}\nu$  is the dynamic viscosity.

The entropy equation (3) amounts to the adiabaticity statement  $D\theta/Dt = 0$ , thanks to the assumption of vanishing thermal diffusivity—the approximation consistent with laboratory studies conducted in saline solutions with large Schmidt numbers. The governing equations are deliberately written in terms of potential temperature and pressure perturbations to facilitate initial and boundary conditions as well as to enable a semi-implicit amplitude-error-free representation of the buoyant modes. To closely link the anelastic equations for low Mach number atmospheric flows with studies addressing marine applications, the governing set (1)-(3) is taken in the incompressible Boussinesq limit with  $\bar{\rho} = \rho_o$ ,  $\bar{\theta} = \theta_o$ , and  $\theta_e(x_3) = \theta_o + Sx_3$ . In this limit—valid for displacements of fluid parcels that are small compared to scale height  $S^{-1}$  of the stratified environment—the equations written in terms of density stratification or potential temperature stratification are mathematically equivalent.

## 2.2 Numerical integration

The governing equations are solved numerically using a semi-implicit NFT-FV solver, presented in comprehensive detail in [51]. Its key components consist of the unstructured and hybrid mesh based MPDATA [40,41] as the nonlinear advection operator, and a robust non-symmetric Krylov-subspace elliptic solver [43] for the Poisson equation for pressure. At the highest level of abstraction, the NFT model algorithm for the prognostic PDEs (2)-(3) can be viewed as an analogue to the trapezoidal integral of the Lagrangian ODEs underlying (2)-(3) [38]. This leads to a 4x4 implicit linear problem of the form

$$\Psi = \widehat{\Psi} + 0.5\delta t \mathbf{R}(\Psi) \quad (5)$$

in each node of a collocated mesh. In (5),  $\Psi$  symbolises the unknown vector of four dependent variables—namely, three components of  $\mathbf{V}$  and  $\theta'$ —at the future  $t + \delta t$  time level,  $\widehat{\Psi}$  marks the explicit part of the solution including advection of the past  $\Psi$  values at  $t$  combined with their corresponding RHS forcings, and  $\mathbf{R}(\Psi)$  symbolises the future RHS forcings comprising the pressure gradient, buoyancy and the convective derivative of the ambient  $\theta_e$ .<sup>1</sup> The linear problem (5) is inverted algebraically in each node, leading to the closed form discrete expression

$$\mathbf{V} = \widehat{\widehat{\mathbf{V}}} - \mathbf{C}\nabla\varphi', \quad (6)$$

where  $\widehat{\widehat{\mathbf{V}}}$  is a modified explicit part of the solution  $\mathbf{V}$ ,  $\mathbf{C}$  is a 3x3 matrix of known coefficients, and  $\varphi'$  is the unknown solution for the pressure variable. Substituting (6) into the discrete form of (1) forms the discrete Poisson problem for  $\varphi'$ . In the spirit of the exact projection, it ensures that the updated velocity  $\mathbf{V}$  can satisfy the discrete mass continuity to a round-off (as opposed to a truncation) error. This is particularly important for simulation of stratified flows, as it assures the compatibility of conservative MPDATA advection with the mass continuity and eliminates fictitious buoyancy forces in regions of locally undisturbed isentropes. The updated velocity is subject to Dirichlet boundary conditions, which implies consistent Neumann boundary conditions on the resulting pressure field. The reader interested in further details of semi-implicit NFT integrators and the associated elliptic solvers is referred to [51,49,39] and references therein.

Spatial discretisation adopts a median-dual finite-volume approach with edge-based connectivity outlined in [50]. The primary meshes employed in this work, illustrated in Fig. 14, combine prismatic elements near solid boundaries and tetrahedral elements elsewhere. The median-dual cell faces are constructed from the primary meshes, where the midpoint of each edge is connected both to the barycentres of the surrounding polyhedra and to the centres of the polygonal faces sharing the edge. Noteworthy is the synergism of the collocated arrangement of all dependent flow variables and the proven ILES property of MPDATA. On one hand, the data collocations enables algebraic inversion of the linear problem (5) at the heart of the semi-implicit NFT integrators, which generally can be quite complex [33,47]. On the other hand, collocated meshes admit non-trivial null spaces of the discrete differential operators, including in particular the generalised Laplacian that forms the viscous terms. The latter can manifest as a noise at fine scales near the limit of mesh resolution, even for low Reynolds number flows that are otherwise well resolved. The solution regularisation at the limit of mesh resolution characteristic of ILES remedies this problem. Importantly, as the MPDATA ILES regularisation is adaptive

---

<sup>1</sup> The dissipative forcing of momentum is integrated to  $\delta t\mathcal{O}(\delta t)$  and included in  $\widehat{\Psi}$ .

(as opposed to additive) to explicit dissipation, it has a negligible impact on the resolved scales [27,28,6]. In effect, our NFT-FV schemes benefit from the collocated data arrangement while being inherently stable even with low-numerical-diffusion [46,51,20].

While NFT codes operating on Cartesian meshes and exploiting the advantages of the distributed memory paradigm are well established, the successful implementations of NFT-FV codes for unstructured meshes on multi-node architectures are more recent. To date these efforts have focused on global models for the Earth’s atmosphere with meshes that are quasi-uniform in the horizontal and prismatic in the vertical [45,20]. In this paper, we complement our earlier work with new NFT-FV model developments that provide capabilities for parallel simulations on fully unstructured, irregular meshes. We utilise the multilevel graph partitioning scheme supplied by the MeTis package [19] to assign partitions of the computational spatial domain. This library effectively balances the sub-domain workloads for irregular meshes, while minimising the number of edges crossing partition boundaries.

The NFT-FV solver utilises a localised stencil on collocated data, and an auxiliary bespoke OpenMP parallelised code configures partition halos, with a halo depth of one. The second order operators found in (1-3) and the Poisson equation therefore require an internal halo exchange after applying first order operators, but benefit from a reduced memory footprint of internal variables. Halos operate on a partition-to-partition exchange basis and halo points are chunked in the data-structure. Most MPI communications exchange information only between immediate neighbours, with some limited global communications as required by the Krylov-subspace solver—all of which utilise the standard MPI library.

### *2.3 Problem formulation*

Simulation results for neutrally and stably stratified flows past a single sphere are discussed first, due to its extensive existing research history and the availability of pertinent data. Following [18,53], the cuboidal computational domain has dimensions  $[-15, 25] \times [-15, 15] \times [-15, 15]$  in units of a solid sphere diameter  $D$  (set to unity) placed at the origin. Within a  $0.2D$  thick region from the sphere surface, the hybrid primary mesh is composed of 10 layers of prismatic elements with triangular bases. Everywhere outside this region, the mesh is composed of tetrahedral elements. The mesh contains 1915318 nodes, with decreasing inter-nodal distance in the proximity of the sphere surface and the flow wake, with the shortest edge length of  $0.005D$ . No-slip boundary conditions are applied on the sphere’s surface and free-slip conditions on the spanwise faces of the domain. A constant free stream velocity

$V_e = V_o = (1, 0, 0) \text{ ms}^{-1}$  is prescribed at the streamwise boundaries of the domain, while absorbers applied at a distance of  $2.0D$  from inlet and outlet boundaries attenuate the solution toward the free stream condition. The potential flow solution initialises all presented simulations.

In the quantitative analysis, the drag  $C_d$ , side force  $C_s$  and lift  $C_l$  coefficients, together with the Strouhal number  $St$ , are used to evaluate the results. For a flow impinging on a sphere, the force coefficients are defined as

$$C_\zeta = \frac{F_\kappa}{0.5\rho_o V_o^2 A} , \quad (7)$$

where  $A = \pi(D/2)^2$  is the reference area, and  $\zeta$  indicates indices  $d, s$  or  $l$ . The forces  $F_\kappa$ —with  $\kappa = 1, 2, 3$  corresponding to drag, side and lift forces acting on the sphere—are computed according to

$$F_\kappa = - \oint \rho_o \varphi n_\kappa dS + \oint \mu \left( \frac{\partial V_\kappa}{\partial x_J} + \frac{\partial V_J}{\partial x_\kappa} \right) n_J dS , \quad (8)$$

where for any index  $\iota$ ,  $n_\iota$  is the  $\iota^{\text{th}}$  component of the unit vector normal to the surface of the face  $dS$  of the finite-volume element and repeating indices imply the summation.

The Strouhal number is defined as  $St = fD/V_o$ , where  $f$  is the frequency of the vortex shedding. Since  $V_o$  and  $D$  are equal to one, the Strouhal number can be directly derived from the frequency spectrum of the relevant coefficient. We also note that for the sphere the Froude and Reynolds numbers become  $Fr = 2V_o/ND$  and  $Re = V_oD/\nu$  respectively.

### 3 Results

#### 3.1 Flow past a sphere at $Re = 200$

The steady state behaviour of a neutrally stratified flow past a sphere at the Reynolds numbers between 20 and 210 is characterised by the axisymmetric flow in the wake region. It is well studied by means of direct numerical simulations [1] and verifiable by experimental observations [52]. Computations with the NFT-FV scheme for  $Re = 200$  and  $Fr = \infty$  are documented in [51]. They show that the resulting drag coefficient  $C_d = 0.774$ , the length  $L_r = 1.42D$  of the steady axisymmetric recirculation bubble behind the sphere, and the boundary layer separation angle  $\phi_s = 116.6^\circ$  are in agreement with values

obtained from the experiment [29] and other numerical studies, e.g. [10,53,1]; see section 4.2 in [51] for further comparisons and references.

In line with [23], the NFT-FV computations indicate that for Froude numbers higher than  $Fr \sim 10$ , the flow resembles the neutrally stratified case; and, as the Froude number decreases the density stratification starts to significantly impact the flow behaviour [26,23,3]. For  $Re = 200$ , three dominant flow patterns have been identified in [23] throughout the Froude number regimes. However, the transitions between these flow patterns are not clearly defined and exhibit intermediate flow features leading to alternative classifications. For example, [13] distinguishes further different flow characteristics for low and moderate Reynolds numbers. Our simulations for a range of  $Fr$  were carried out using the NFT-FV scheme until flow patterns have been established. The non-dimensional simulated time of  $T = t V_o/D = 30$  was used in [51]. The parallel implementation of the scheme enabled fivefold  $T = 150$  to tenfold  $T = 300$  extensions of the simulated time, used in this work.

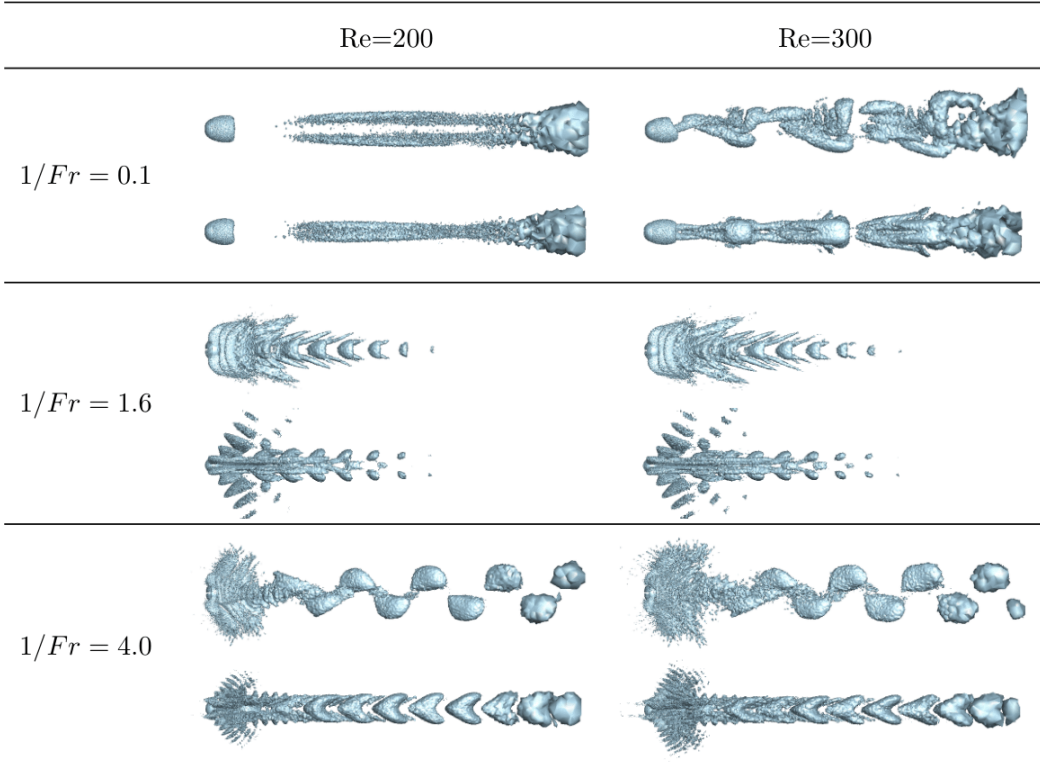


Fig. 1. A visualisation of the wake vortex structures at  $Re = 200$  (left) and  $Re = 300$  (right). For each case the upper and lower images illustrate the flow in the horizontal and vertical central planes, respectively.

Numerical simulations of stably stratified flows past a sphere for moderate Reynolds numbers, especially for  $Re = 200$ , have been reported before (e.g. [30,13,31,32,22,14]) but, to the best of our knowledge, this study together with our earlier investigation in [51] are the first to document such simulations

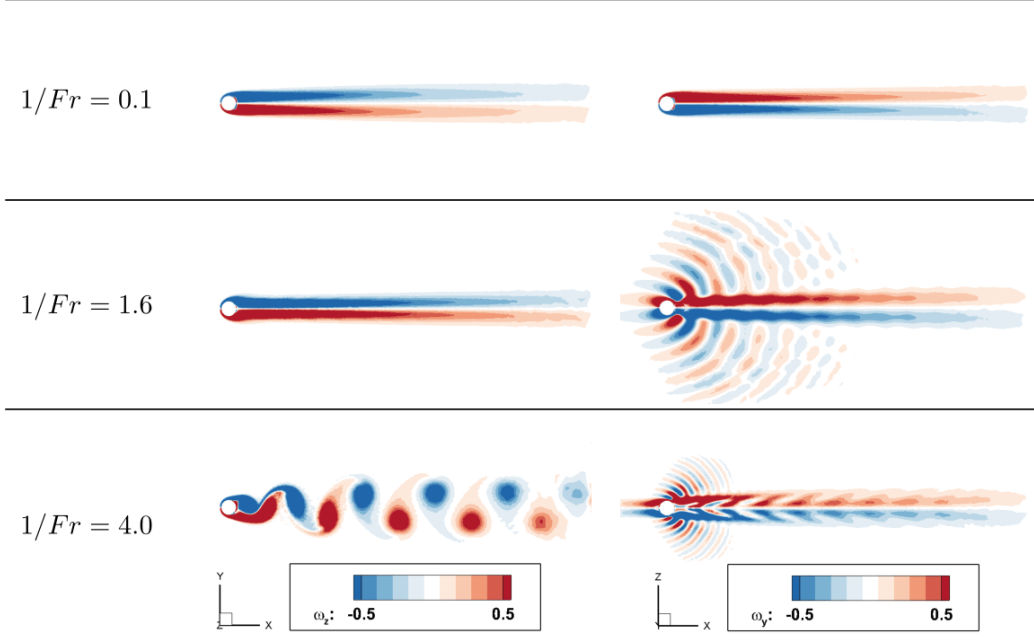


Fig. 2. Contours of instantaneous vorticity (components normal to the figure plane) of the wake vortex structures at  $Re = 200$  for  $1/Fr = 0.1, 1.6, 4$  in central horizontal and vertical plane on the left and right, respectively.

using unstructured meshes. The results presented here have been carefully selected to enable their verification against the existing experimental and numerical data and to provide a systematic illustration of the quality of solutions achievable on unstructured meshes, for the distinct flow regimes occurring at  $Fr \in [0.1, \infty]$ . Especially noteworthy features covered in the following examples are: cases of symmetrical flows obtained on fully irregular meshes, the ability of unstructured meshes to capture detailed flow features, and an excellent accuracy of the computed drag.

Figure 1 shows an instantaneous level set of the positive second invariant of the deformation tensor;  $Q = 0.5(\Omega_{IJ}\Omega_{IJ} - \mathcal{D}_{IJ}\mathcal{D}_{IJ})$ , where  $\mathcal{D}_{IJ}$  is half of the tensorial part of (4), and  $\Omega_{IJ} = 0.5(\partial V_I/\partial x_J - \partial V_J/\partial x_I)$  are entries of the rotation tensor. This presentation is known as the  $Q$ -method for vortex identification [17]. The left column in Fig. 1 illustrates the 3D structures of the wake flow obtained for  $Re = 200$  in horizontal and vertical planes at the reciprocal Froude numbers  $1/Fr = \{0.1, 1.6, 4\}$ ,<sup>2</sup> representative of the three flow patterns identified in [23]. Figure 2 illustrates the corresponding vorticity patterns. For the consecutively increasing values of  $1/Fr$  the three patterns represent, respectively, a non-axisymmetric attached vortex, lee-wave instability, and two-dimensional vortex shedding. They are in agreement with the experimentally-based schematics provided by Figs. 2 and 3 in [23].

<sup>2</sup> Consider that  $1/Fr$  can be thought of as a normalised dominant wave number.

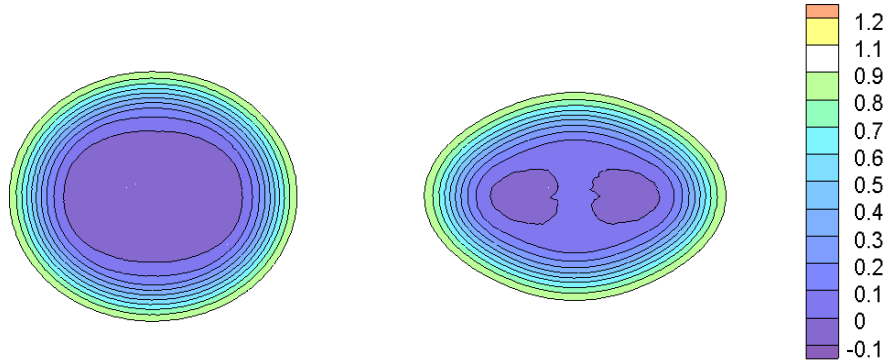


Fig. 3. Contours of streamwise velocity component in the  $x = 0.51$  plane;  $Re = 200$ ,  $1/Fr = 0.4$  (left) and  $1/Fr = 0.8$  (right) with respective (horizontal, vertical) axes equal  $(1.42, 1.23)$  and  $(1.48, 1.02)$ .

Due to the buoyancy-induced gravity waves radiating in the lee, even for weak stratification  $1/Fr = 0.1$ , the flow past a sphere loses its axisymmetric character even though viscous effects are still strong. Planar symmetry of the wake can be observed separately in the horizontal and vertical central planes in both the 3D images and vorticity plots, representing a steady recirculation bubble formed behind the sphere. Noteworthy, the symmetry of the solution is not affected by the use of irregular unstructured meshes. As the Froude number decreases, the separation point on the vertical plane moves towards the rear of the sphere [23] and the breaking of axial symmetry becomes more pronounced. In particular, at  $1/Fr = 0.4$  the vertical deformation results in a characteristic doughnut-shaped attached vortex, illustrated in the streamwise velocity plot at the  $x = 0.51$  plane in the left image of Fig. 3. At  $1/Fr = 0.8$  the increased stratification causes further deformation, such that the doughnut-shaped vortex becomes doubly connected, leaving two attached vortices as shown in the right image of Fig. 3. These results confirm the three-dimensional interpretative experimentally-based sketches in Figs. 20a,b in [23]. Similarly to the experimental observation (Fig. 19) and corresponding sketch (Fig. 20c) in [23], at  $1/Fr = 0.8$  the NFT-FV computations indicate the formation of the bulge-like particle streak pattern (not shown).

The bulge-like particle streak pattern also occurs at  $1/Fr = 1$ , when the lee-wave amplitude approaches its maximum. Figure 4 presents the streamwise velocity plots and the associated streamlines at the planes  $z = 0$  and  $y = 0$ . The bulge-like particle streak pattern can be clearly seen in the lower panel and the streamlines show that the flow remains attached to the sphere, while the separation angle moves towards the aft stagnation point. The patterns represent a transition between the non-axisymmetric and the lee waves instability regimes. They are in good agreement with those observed experimentally; cf. Fig. 18 ( $Re = 859$ ,  $1/Fr = 1.16$ ) in [23], Fig. 1b ( $Re = 287$ ,  $1/Fr = 1.136$ ) in [15], and Fig. 6iv ( $Re = 329$ ,  $1/Fr = 1.11$ ) in [3]. The flow patterns in the

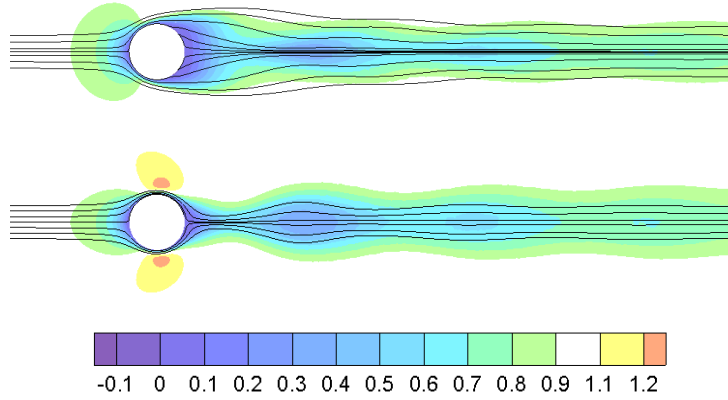


Fig. 4. Contours of streamwise velocity component and the associated streamlines plotted in the planes  $z = 0$  (top) and  $y = 0$  (bottom), respectively;  $Re = 200$  and  $1/Fr = 1$ . Streamwise direction extent is  $x \in [-2.7, 10.4]$  (the same in all akin figures).

horizontal and vertical planes are now distinctly different. The special case of  $Fr = 1$  is further discussed in [51] in the context of the dividing streamline [16] and the linear theories. Consistently with results reported in [3], at  $1/Fr \approx 1.2$ , the wake collapses resulting in a “bow-tie”-shaped separation line, with a bulge at a distance of  $1.5D$  from the rear stagnation point.

The propagation of the lee waves becomes profound between  $1/Fr = 1.6$  and  $1/Fr = 2$ . The 3D plots in Fig. 1, vorticity patterns in Fig. 2, and the streamwise velocity components plots with associated streamlines in Fig. 5 were obtained for  $1/Fr = 1.6$ . They are representative of the lee-wave instability regime and show similar features to experimental patterns in Fig. 14 ( $Re = 500$ ,  $1/Fr = 2.63$ ) in [23], Figs. 6ii,iii ( $Re = 329$ ,  $1/Fr = 1.66$ ) in [3], and Fig. 1a ( $Re = 144$ ,  $1/Fr = 2.27$ ) in [15]. Here, the concept of the dividing streamline becomes relevant to the resulting flow pattern. The fluid parcels above the height of the dividing streamline have sufficient kinetic energy to flow over the top of the sphere and, due to the presence of lee waves, have a down-slope velocity greater than the mean stream; cf. [3]. The attached recirculation becomes elongated, Fig. 5, while the lee waves in the vertical centre-plane are clearly visible, although dissipated further downstream. The characteristic overturning motion of fluid parcels, due to the combined effects of buoyancy and shear [3,23], are represented by tiny recirculation regions that can be seen in the lower image of Fig. 5. They give the name to the “lee-wave instability regime” [23].<sup>3</sup>

Further increasing the stratification results in a predominantly two-dimensional

<sup>3</sup> Note that the streamline plots are constructed from data stored on irregular meshes, which affects their symmetry.

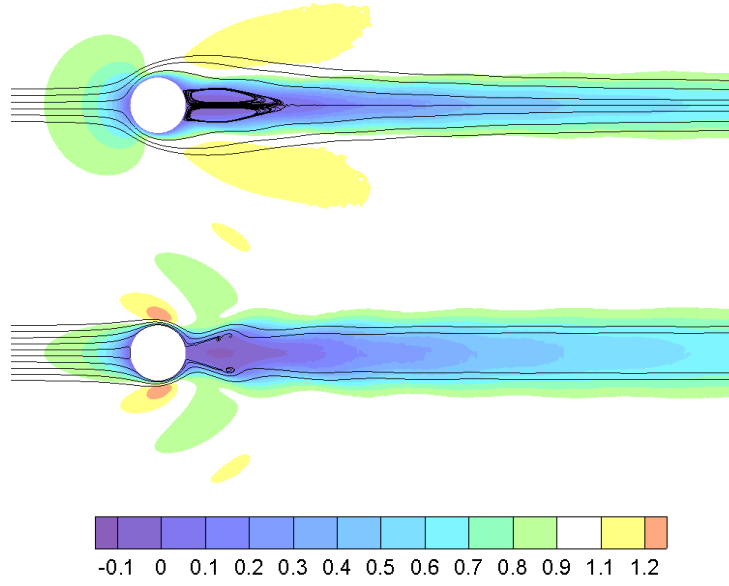


Fig. 5. Contours of streamwise velocity component and the associated streamlines plotted in the planes  $z = 0$  (top) and  $y = 0$  (bottom), respectively;  $Re = 200$  and  $1/Fr = 1.6$ .

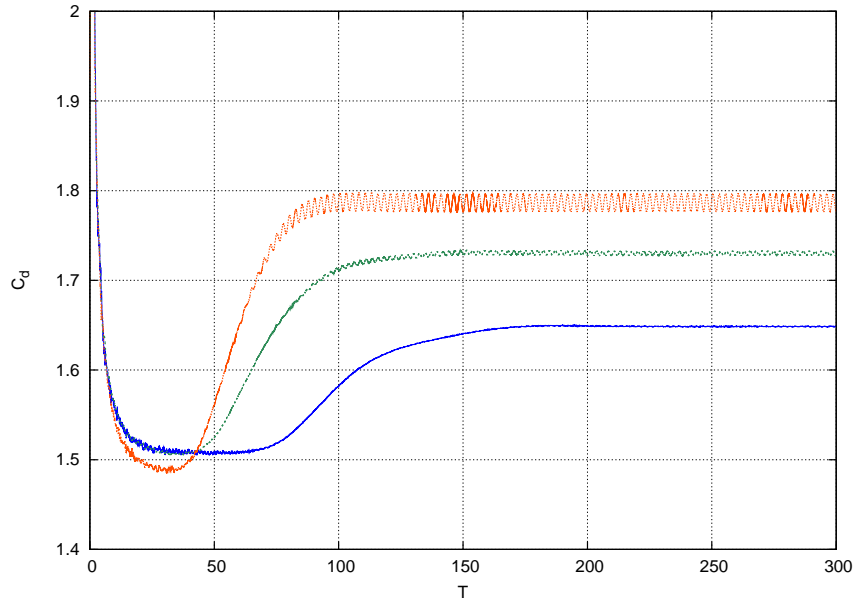


Fig. 6. Drag coefficient,  $C_d$  in (7), history for  $Re = 200$  and  $1/Fr = 2.25, 2.5, 3$  respectively marked with solid (blue), dashed (green) and dotted (red) lines.

flow pattern in the vicinity of the  $z = 0$  plane, with vertical motions that become weaker as the stratification increases. Moreover, computations indicate that starting from about  $1/Fr = 2.25$ , the flow loses the steadiness characteristic of the neutrally stratified flow at  $Re = 200$ . The influence of selected stratification levels on the drag coefficient  $C_d$  is illustrated in Fig. 6 for computations simulating the non-dimensional time  $T = 300$ . The figure shows

that the time from the model initialisation to the onset of flow periodicity depends on the stratification. For  $1/Fr = 2.25$  the periodicity of the flow is hardly visible, as the amplitude in the  $C_d$  plot is almost one order smaller than for  $1/Fr = 2.5$ . However, examination of the corresponding streamlines and streamwise velocity at the central horizontal plane, Fig. 7 top, reveals that the periodic two-dimensional vortex shedding already takes place at  $1/Fr = 2.25$ , while for  $1/Fr = 2$ , Fig. 7 bottom, the flow is still steady but its symmetry in the horizontal plane has been already broken.

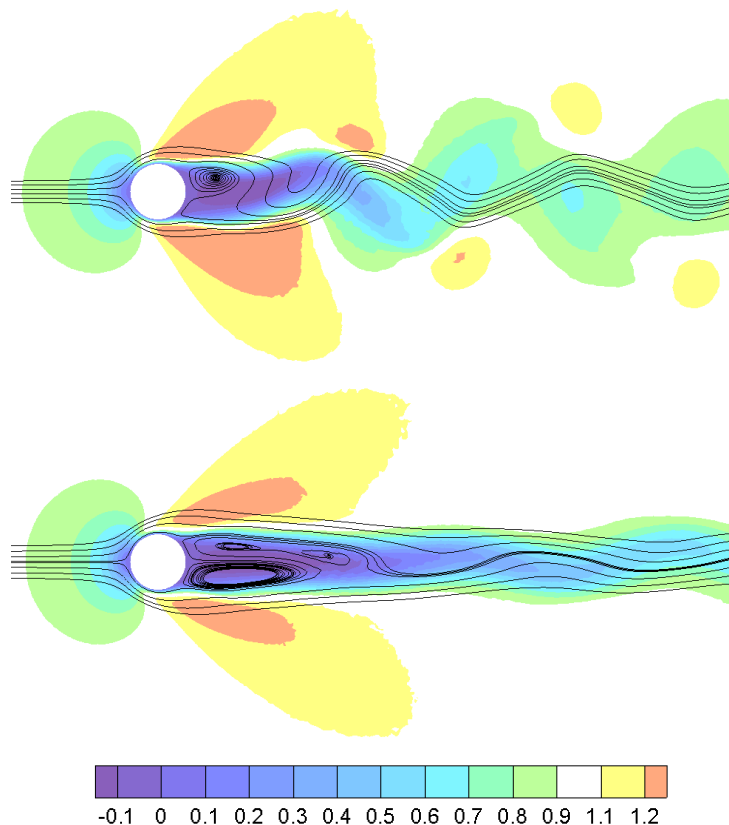


Fig. 7. Streamwise velocity component and the associated streamlines in the  $y = 0$  plane;  $Re = 200$ ,  $1/Fr = 2.25$  (top) and  $1/Fr = 2$  (bottom).

The NFT-FV results confirm the experimental [23] and numerical [12] findings reporting that the flow remains stationary until  $1/Fr \approx 2.5$ , while computations in [22] indicate that the flow remains stationary for  $1/Fr < 2$ . At  $1/Fr = 4$ , illustrated in Figs. 1 and 2, the flow follows a distinct two-dimensional vortex shedding pattern in the horizontal central plane. The fluid parcels in the central part of the flow, between the dividing streamlines, do not have sufficient kinetic energy to travel over and under the sphere. Strong stratification forces them to flow around, resulting in a motion similar to a flow around a cylinder. In contrast, the parcels travelling above and below the dividing streamlines appreciate the obstacle as a hill of a moderate height which gives rise to the vertical pattern of linear gravity waves characteristic of

flow past isolated mountains. Both horizontal and vertical patterns are clearly visible in Figs. 2 and 1. For  $1/Fr = 4$  the vorticity plots illustrate a significant decrease of the gravity waves' amplitudes and lengths by comparison with results obtained for  $1/Fr = 1.6$ . Similar patterns to those shown in Fig. 1 for this flow regime were obtained both computationally (Figs. 5c-d in [13]) and experimentally (Fig. 10e in [23], and Fig. 5a in [3] with  $Re = 1961$ ).

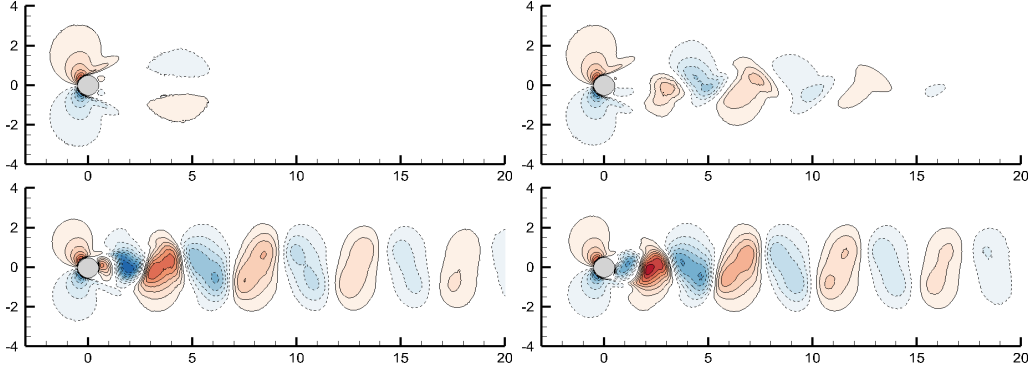


Fig. 8. Evolution of the transverse velocity at the  $z = 0$  plane;  $Re = 200$ ,  $1/Fr = 4$ . The solid and dashed lines correspond to strictly positive and negative values, marked with contour interval  $0.1V_0$ . Going clockwise from the upper left panel, the corresponding dimensionless times are  $T = 30, 62.5, 125$ , and  $150$ .

The computations for  $1/Fr = 4$  in [51] used a serial code and, following [14], adopted the non-dimensional simulation time  $T = 30$ . The current results show that for stratifications with  $1/Fr > 2.5$ , a longer simulation is required to trigger a transition from a steady to an unsteady pattern. The four panels in Fig. 8 illustrate the evolution of the flow pattern for  $1/Fr = 4$  that gradually transitions from the symmetric steady state reported in [14] to a quasi-two-dimensional vortex shedding. In experimental and computational studies, the transition to unsteady flow is typically triggered by arbitrary perturbations. Indeed, the addition of a white noise with amplitude  $0.2V_0$  introduced into the potential flow initialisation substantially accelerates the transition, and the onset of shedding is sensitive to the magnitude of the perturbations, Fig. 9. However, after long simulation times, all computed flows developed the same vortex shedding pattern as that shown for  $T = 150$  in Fig. 8. Furthermore, a deliberate test replacing the second-order-accurate MPDATA in the NFT-FV solver with an over-diffusive first-order upwind scheme, shows that excessive numerical diffusion can entirely prevent the transition to an unsteady flow regime. Physically this is not surprising as the onset of shedding is related to the viscous boundary layer separation whereas the established flow depends robustly on the Reynolds and Froude numbers. Numerically, however, these results attest to the solution quality and robustness on the unstructured non-symmetric meshes.

Following [14], the influence of stratification on the drag is quantified in terms of the departure of the drag coefficient  $\Delta C_d = C_d(Re, 1/Fr) - C_d(Re, 0)$  from

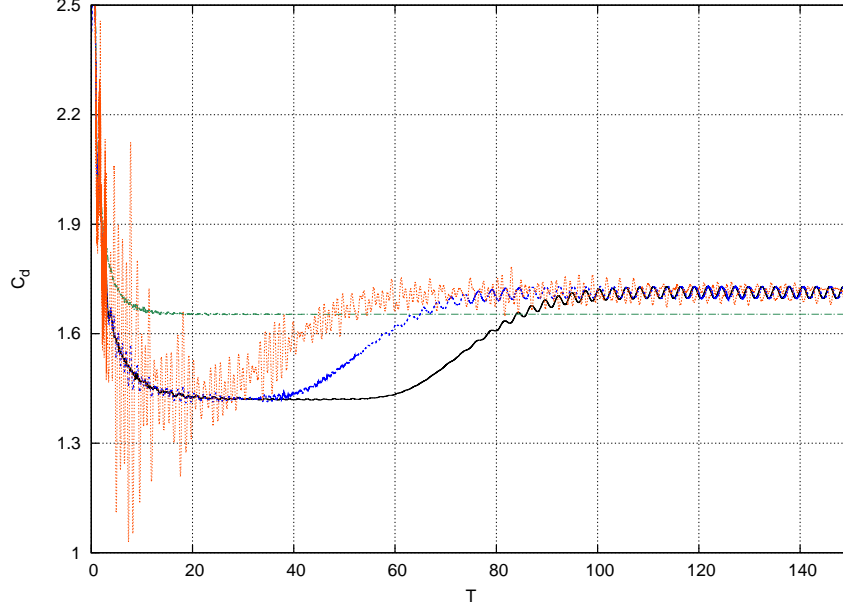


Fig. 9. Comparison of the drag coefficient histories for the reference setup (solid black) with analogous setups but with noisy initial conditions: noise amplitudes  $0.2V_o$  (dashed blue) and  $2V_o$  (dotted red), respectively, and the first-order-accurate upwind advection in lieu of MPDATA (dashed-dotted green);  $Re = 200$  and  $1/Fr = 4$ .

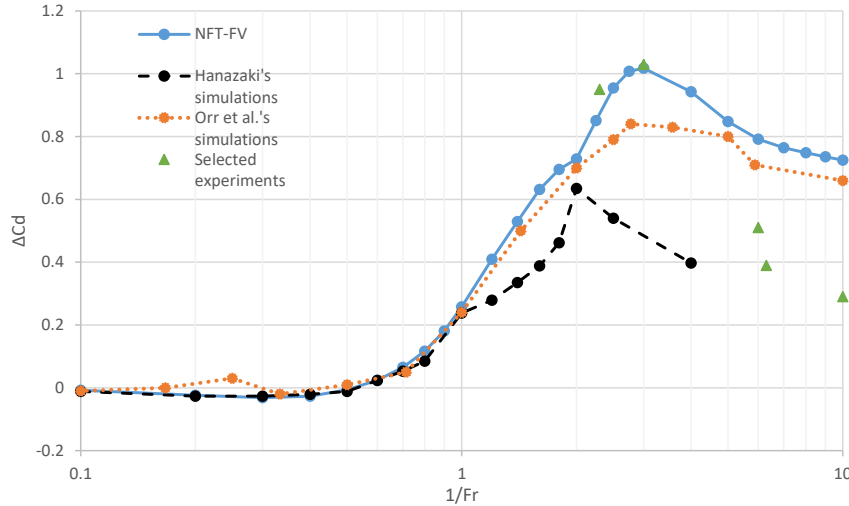


Fig. 10.  $\Delta C_d$  in function of the inverse Froude number  $1/Fr$  for numerical solutions at  $Re = 200$ , NFT-FV (solid blue), [14] (dashed black), and [30] (dotted orange) as well as the experimental data [26] (green triangles).

its value for the neutrally stratified flow. Figure 10 compares our calculations for  $1/Fr \in [0, 10]$  with the results obtained experimentally in [26], and computationally in [14] and [30]. For unsteady flows the drag coefficient in our calculations was averaged over the time interval  $T \in [100, 150]$ . Since the experimental data in [26] were obtained at varying Reynolds numbers, Fig. 10 shows their results only from the experiments at  $Re$  closest to 200. For clarity,

these values are listed in Table 1. Up to  $1/Fr = 1$ , all results are in good agreement. For  $1/Fr \in [0.1, 0.5]$ , the stratification is weak, so  $\Delta C_d$  remains close to zero. For  $1/Fr > 1$  the results of [14] show a significant departure from other data. For  $1/Fr \in [1, 2]$ , the remaining computations are in excellent agreement. In the range  $1/Fr \in [2, 3]$ , the NFT-FV results match the experimental values closely and show an increasing slope. At  $1/Fr = 3$ , the results from experiment, computation of [30] and the current simulation all show a sharp decrease in slope. This change of regime is consistent with the linear theory of [35,36] and the numerical/laboratory results in [37,55]. Between  $1/Fr \in [3.5, 5]$ , experimental data is only available for different Reynolds numbers, however, both [30] and the current NFT-FV computations show similar decreasing slope tendencies as the experiments in [26]. For  $1/Fr \in [5, 10]$ , both computations give comparable results but their departure from the experiments is significant. The authors in [30] attribute this to an insufficient mesh resolution for a strong stratification which could also be a factor affecting the NFT-FV results. We shall return to this issue in section 4.

Table 1  
 $\Delta C_d$  values of [26] used in Fig. 10.

$1/Fr$		2.3	3	6	6.3	10
$\Delta C_d$		0.95	1.03	0.51	0.39	0.29
$Re$		183	221	226	215	191

Further quantitative analysis compares the Strouhal numbers evaluated from the periodic evolution of the drag and side force coefficients at  $1/Fr = 3, 5, 10$ . Table 2 displays the NFT-FV results together with the corresponding outcome obtained in [22]. The results are in good agreement overall, with the magnitude of  $St$  evaluated from the drag coefficient being typically twice as large as that reached by  $St$  computed from the side force coefficient. The latter is consistent with an interpretation of the 2D vortex shedding from the sphere being akin to the vortex shedding in a flow past a cylinder [22]. The Strouhal numbers evaluated from the lift coefficients (not shown) obtained by the NFT-FV scheme are close to those obtained from the side force coefficients.

Table 2  
 Strouhal numbers based on  $C_d$  and  $C_s$  coefficients (cf. [22]).

$1/Fr$		10 (10)	5 (5)	3 (3.3)
$St(C_d)$		0.395 (N/A)	0.376 (0.398)	0.395 (N/A)
$St(C_s)$		0.198 (0.202)	0.198 (0.196)	0.198 (0.172)

### 3.2 Flow past a sphere at $Re = 300$

As observed experimentally (Figs. 39a,b in [18]) and numerically (e.g. Fig. 2c in [13]), the neutrally stratified flow past a sphere at  $Re = 300$  results in periodic vortex shedding. The drag coefficient obtained from our NFT-FV simulation for  $Re = 300$  and  $1/Fr = 0$  is evaluated by averaging the drag force over the non-dimensional time interval between  $T = 250$  and  $T = 300$ . Its mean value  $C_d = 0.664$  and oscillation amplitude  $C'_d = 0.002$  are consistent with the results in [51] and the references therein. The Strouhal number derived from the frequency spectra of instantaneous  $C_d$  is  $St = 0.138$ . It compares well with  $St = 0.136$  and  $St = 0.137$  reported in [18,4] and [53,57], respectively.

For weak stratification,  $1/Fr = 0.1$ , the character of the neutrally stratified flow vortex pattern is maintained; see Fig. 1 illustrating 3D features in the near wake and contrasting them with a distinctly different  $1/Fr = 0.1$  flow at  $Re = 200$ . The units of the periodic wake structure consist of hairpin vortices with planar symmetry preserved in time and set by the incipient shedding. Three vortex-shedding structures can fit in the adopted computational domain. As the stratification increases the vortex shedding is suppressed and the flow becomes close to steady-state, Fig. 11, apart from tiny recirculation regions that form due to the combined effects of buoyancy and shear, just like for  $Re = 200$ . Figure 1 shows that for lower Froude numbers,  $1/Fr = 1.6$  and 4, stratification dominates viscous effects and the flow patterns for  $Re = 200$  and  $Re = 300$  become close. The results for Froude numbers where the lee-wave instability regime occurs are also similar for both Reynolds numbers, with the lee-waves pattern being already well-developed at  $1/Fr = 1.6$ . However, for  $Re = 300$  the change from the lee-waves instability into two-dimensional vortex shedding structure occurs around  $1/Fr = 1.8$ ; i.e. earlier than for  $Re = 200$ . Furthermore, a closer inspection of Figs. 11 and 5 shows that at the same  $1/Fr = 1.6$ , the length of the steady recirculation formed behind the sphere in the horizontal plane increased by comparison with that measured for the  $Re = 200$  case.

Figure 12 compares the NFT-FV results with the experiment [26] for  $\Delta C_d$  as a function of  $1/Fr$ . As for the case of  $Re = 200$ , the drag coefficient in the NFT-FV calculations was averaged over the time interval  $T \in [100, 150]$ . Only the data for the Reynolds numbers close to 300, listed in Table 3, are shown in the graph. The results are well matched for  $1/Fr = 1.8$  and display appropriate slope changes up to  $1/Fr \sim 3$ . The results for  $1/Fr = 3$  and  $1/Fr = 4$  are close to the experimental values. Notably, the experimental result for  $1/Fr = 3.6$  does not follow the slope defined by experiments at  $1/Fr = 3$  and  $1/Fr = 4$ . This and the similar discrepancy for  $1/Fr = 4.8$  are possible manifestations of the magnitude of experimental uncertainty. However when  $1/Fr > 5$ , the decline of the slope for the simulation results is system-

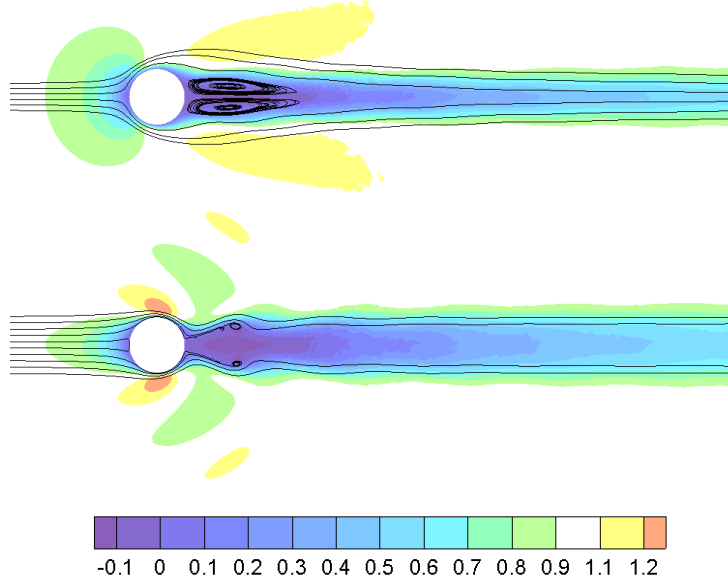


Fig. 11. Contours of streamwise velocity component and the associated streamlines plotted in the planes  $z = 0$  (top) and  $y = 0$  (bottom), respectively;  $Re = 300$  and  $1/Fr = 1.6$ .

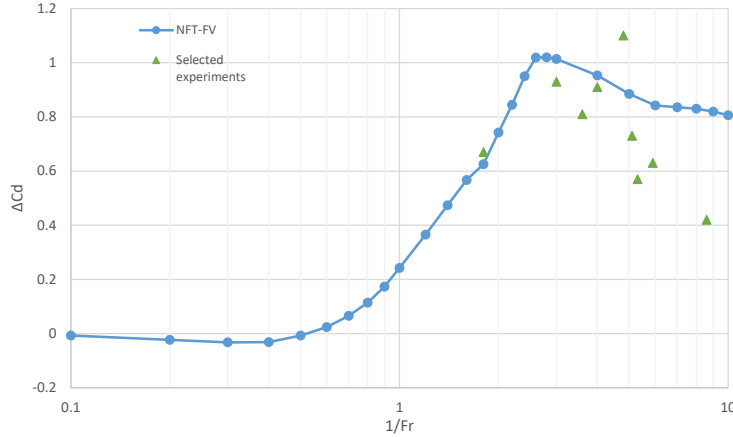


Fig. 12.  $\Delta C_d$  in function of the inverse Froude number  $1/Fr$  for numerical solutions at  $Re = 300$ ; NFT-FV calculations (blue line) and experimental data of [26] (green triangles).

atically shallower than in the experiment. A direct comparison of  $\Delta C_d$  for  $Re = 200$  and  $Re = 300$  (not shown), revealed differences for  $1/Fr \in [1.2, 1.8]$  which could be associated with an earlier change to the two-dimensional vortex shedding regime at  $Re = 300$ . Differences are also present for strongly stratified flows at  $1/Fr \in [5, 10]$ . These are expected since Fig. 1 indicates that the amplitude of lee waves for  $Re = 300$  in the vicinity of the sphere is larger than for  $Re = 200$ . Furthermore, a larger physical viscosity elicits a delayed development of a periodic vortex shedding. For example, for  $1/Fr = 4$  the transition to the fully developed periodic flow takes place at  $T \approx 100$  for

Table 3

$\Delta C_d$  values of [26] used in Fig. 12.

$1/Fr$		1.8	3.	3.6	4	4.8	5.1	5.3	5.9	8.6
$\Delta C_d$		0.67	0.93	0.81	0.91	1.1	0.73	0.57	0.63	0.42
$Re$		331	326	272	339	283	319	251	318	263

$Re = 200$  but occurs at  $T \approx 60$  for  $Re = 300$ .

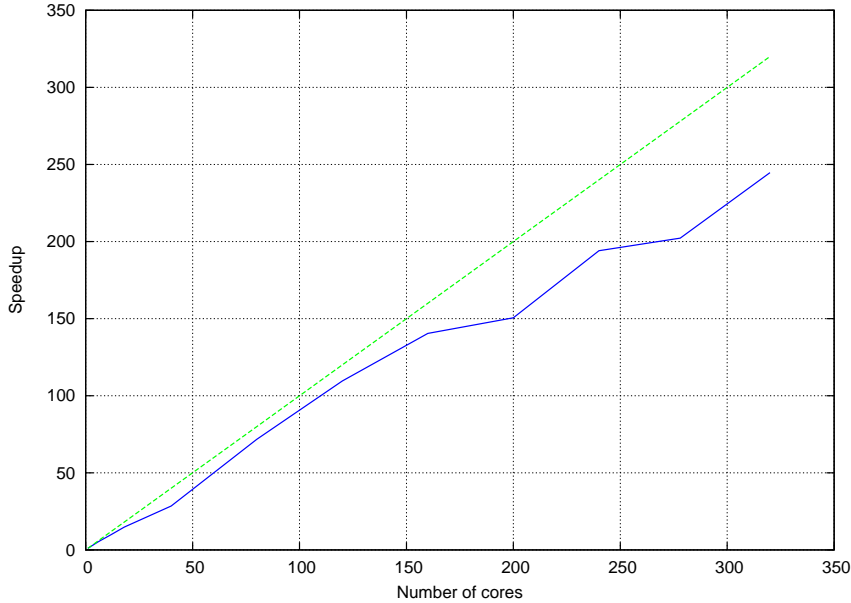


Fig. 13. Scaling results for the MPI parallelised NFT finite-volume code, for  $Re = 300$ ,  $Fr = 1$ ; dotted line shows ideal scaling.

The new parallel implementation of the NFT-FV code operating on fully unstructured meshes was extensively tested for the flow past a sphere at  $Re = 300$ . The computational mesh employed in the presented calculations (described in §2.3) is highly irregular, with the node spacing varying from  $0.005D$  in proximity to the sphere surface to  $1.00D$  at the outer boundaries of the model domain. Figure 13 highlights the code’s speed-up, tested for  $Re = 300$  and  $Fr = 1$ . The speed-up ratio  $T_1/T_N$ , compares the computational time of the sequential and the  $N$ -processes runs needed to complete the simulation. The NFT-FV code shows good scaling until 160 cores, where the parallel efficiency is 0.88 on Hydra’s Intel Xenon CPU E5-2680v2 HPC. <sup>4</sup> Beyond that, the parallel performance becomes affected by the limitations of the mesh size and partitioning variables of the MeTis library.

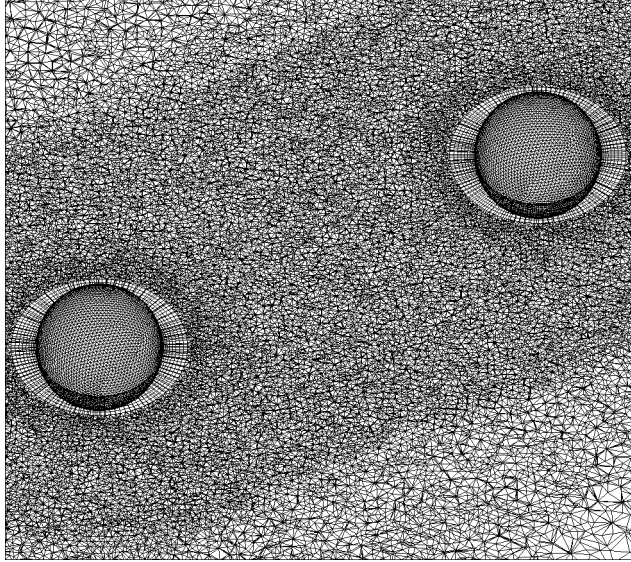


Fig. 14. A fragment of the  $y = 0$  cross-section of the primary mesh for a flow past two spheres and the triangular surface mesh.

### 3.3 Flow past two spheres

To illustrate flexibility of unstructured meshes, the NFT-FV solver was applied to simulate flows past two spheres at  $Re = 300$ . Two identical,  $D = 1$ , spheres were placed in a tandem arrangement aligned with a free stream flow. The coordinates of the first sphere's centre are  $(0, 0, 0)$ , while the centre of the second sphere is located at  $(4, 0, 0)$ . To allow the flow to fully develop downstream of the second sphere, the computational domain is extended to form a cuboid  $[-15, 29] \times [-15, 15] \times [-15, 15]$ . The hybrid computational mesh, shown in Fig. 14, is built in the same way as for the single sphere domain, with 10 triangular base prismatic layers added around each sphere. The mesh consists of 1927331 nodes which are more densely concentrated around and inbetween the two spheres and in the wake regions. The smallest distance of  $0.005D$  between points corresponds to the thickness of the first prismatic layer from the sphere surfaces, while the largest elements of the primary mesh reach the approximate dimensions of  $1D$  near the outer boundaries. This configuration and setup have been chosen to facilitate a quantitative comparison with the neutrally stratified flow solution at  $Re = 300$  in [57].

The neutrally stratified flow past the two spheres was simulated for  $T = 400$ . Figure 15 shows the streamline plot in the vertical central plane,  $y = 0$ . The streamlines reveal non-symmetric recirculations in the lee of both spheres. The shear layer generated by the windward sphere becomes reattached to the second sphere and interacts with the second sphere's boundary layer. This

<sup>4</sup> <http://hpc-support.lboro.ac.uk/>

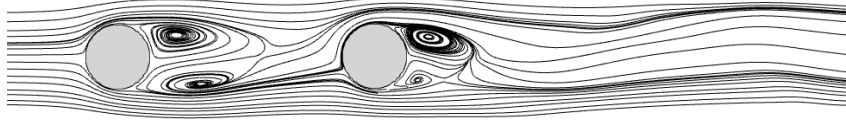


Fig. 15. Streamline plot in the central vertical plane for the  $1/Fr = 0$  flow past two spheres at  $Re = 300$ . Streamwise direction extent is  $x \in [-1.7, 11.5]$ .

affects the wake behind the second sphere and decreases the size of the largest recirculation by a factor of 0.58 in comparison with the analogous single sphere case.

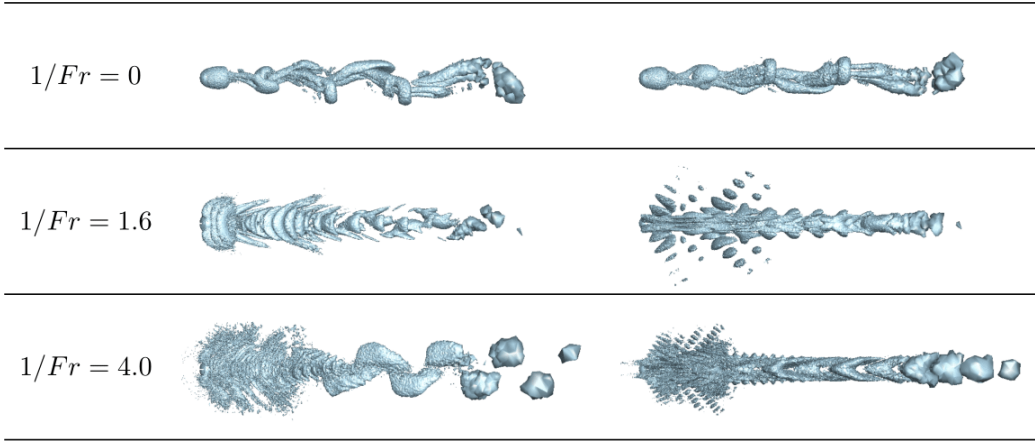


Fig. 16. Flow past the tandem spheres at  $Re = 300$  and  $1/Fr = 0, 1.6, 4$ ; wake vortex structures in the horizontal (left) and vertical (right) central planes.

The upper row of Fig. 16 displays the 3D flow pattern obtained for  $Re = 300$  and  $1/Fr = 0$ . The  $Q$ -method visualisation shows that the hairpin vortices characteristic of the Reynolds number 300 flow past a single sphere (cf. [51]) are also developing in the present case. Furthermore, the right panel clearly shows how the wake generated by the first sphere overlaps the second sphere. Similarly, as with the single sphere in [51], the symmetry plane for the tandem configuration for the neutrally stratified flow is formed in the diagonal plane, rotated  $45^\circ$  about the  $X$ -axis. Notably, even a weak stratification imposes the vertical position of the symmetry plane; cf.  $Re = 300, 1/Fr = 0.1$  case in Fig. 1.

Multiple vortex-shedding frequencies for each sphere were reported in [57]. The left panel of Fig. 17 shows the history of the lift coefficient obtained for both spheres. Frequencies from the NFT-FV simulation match closely those of Fig. 16 in [57]. The phase is shifted due to different initial conditions and the amplitude differs slightly due to the rotation of the symmetry plane in our calculations. The right panel complements the left panel with the history of the drag coefficient. The corresponding mean drag coefficients are  $C_d = 0.632$

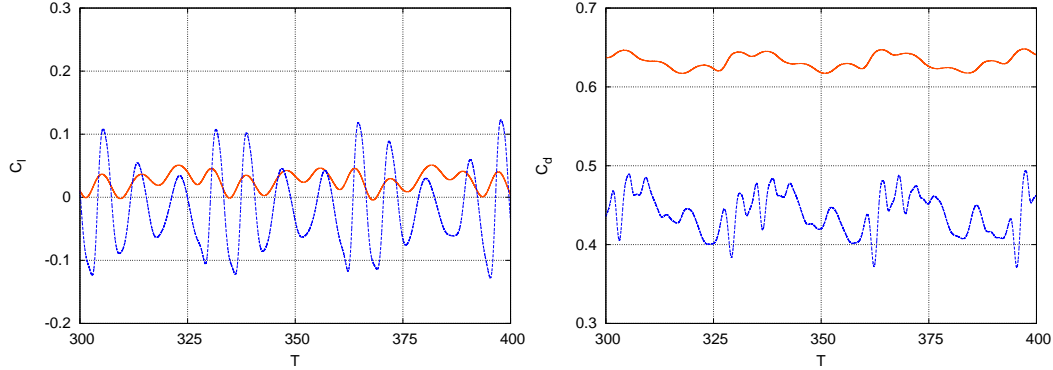


Fig. 17. History of the lift (left) and drag (right) coefficients in  $Re = 300$  and  $1/Fr = 0$  flow past two spheres; solid (red) and dashed (blue) lines correspond to the first and second sphere values.

and  $C_d = 0.439$  for the first and second sphere respectively.

Two dominant vortex-shedding frequencies  $f_1$  and  $f_2$  are found for each sphere. Table 4 provides the Strouhal numbers  $St_1 = f_1 D/V_o$  and  $St_2 = f_2 D/V_o$ , where  $f_1$  and  $f_2$  are derived from the frequency spectra of both drag and lift coefficients (not shown) in the time interval  $T \in [300, 400]$ . They are in a good agreement with those reported in [57]. Overall, these results reflect the influence of the first sphere's leeward flow reattachment in generating the vortices behind the second sphere.

Table 4

Strouhal numbers for the  $Re = 300$ ,  $1/Fr = 0$  flow past two spheres.

	First sphere		Second sphere	
	$St_1$	$St_2$	$St_1$	$St_2$
NFT-FV( $C_d$ )	0.119	0.030	0.089	0.030
NFT-FV( $C_l$ )	0.119	0.030	0.119	0.149
[57]( $C_l$ )	0.122	0.030	0.122	0.153

The flow past two spheres is dramatically influenced by the strength of stratification, as was previously observed for the single sphere. For  $1/Fr = 1.6$ , the symmetric steady state flow is established demonstrating the features characteristic to the lee-wave instability regime behind both spheres, Fig. 18. Consistent with the single sphere case, the vertical scales are inhibited by the stratification. Additionally, in comparison to Fig. 11 the length of steady recirculation formed behind the first sphere in the horizontal plane is approximately one diameter longer and stretches in the entire gap between the spheres. The recirculation after the second sphere is smaller and closer in length to the single sphere recirculation length. The drag coefficients computed for the first and

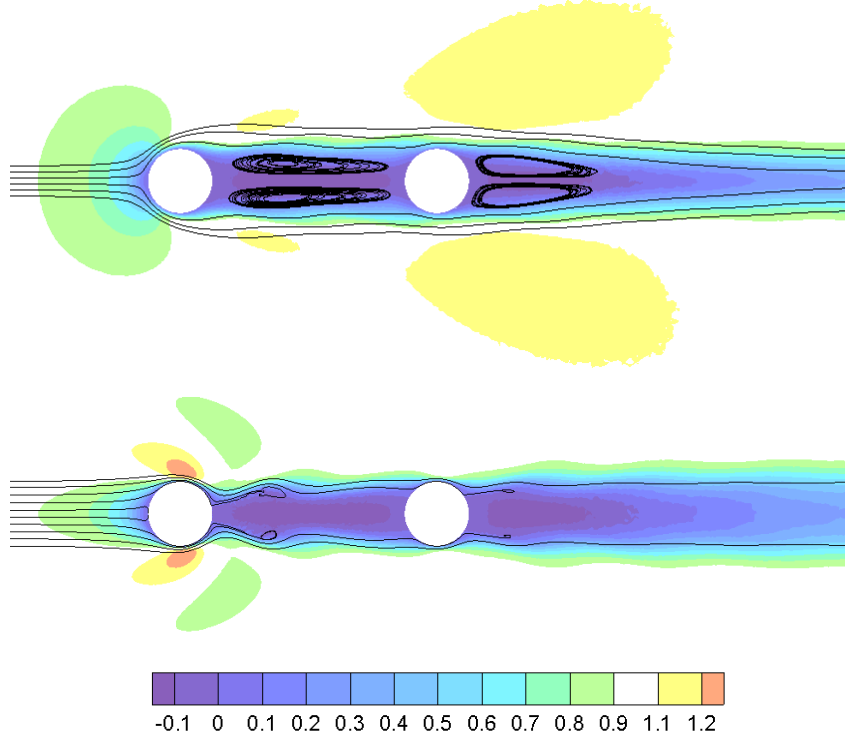


Fig. 18. Contours of streamwise velocity component and the associated streamlines plotted in the planes  $z = 0$  (top) and  $y = 0$  (bottom), respectively;  $Re = 300$  and  $1/Fr = 1.6$ .

the second sphere are  $C_d = 1.100$  and  $C_d = 0.531$ .

Boundary layer separates behind both spheres, as shown in the lower panel of Fig. 18 for a vertical cross-section at  $y = 0$ . The separation angles, denoted by  $\phi_s$ , are measured clockwise from the upstream centerline on the vertical plane, where  $\phi_s = 164^\circ$  and  $\phi_s = 145^\circ$  for the first and second sphere respectively. In comparison, the separation angle for the single sphere at the same Reynolds and Froude numbers (Fig. 11) is  $\phi_s = 166^\circ$ , demonstrating that the separation angles behind the first sphere and the single sphere are similar. The first sphere blocks the incoming flow slowing down its motion between the spheres, and the flow separation limits the width of the wake induced by the first sphere. These two factors lead to a substantially reduced separation angle for the second sphere.

Similarly, for the strongly stratified flow at  $1/Fr = 4$ , the separation angle for the first sphere,  $\phi_s = 131^\circ$ , is higher than for the second sphere,  $\phi_s = 121^\circ$ , while the value for first sphere is lower than  $\phi_s = 138^\circ$  observed for the corresponding flow past a single sphere. The middle and bottom panels of Fig. 16 show 3D plots for flows with  $1/Fr = 1.6$  and 4. The two-dimensional vortex-shedding regime at  $1/Fr = 4$  also preserves the main features of the flow past a single sphere. As was observed for  $1/Fr = 0$  and 1.6, the mean

drag coefficients for  $1/Fr = 4$  evaluated for the first sphere,  $C_d = 1.477$ , is close to that obtained for the single sphere case. However, the mean drag coefficient computed for the second sphere,  $C_d = 0.960$ , is significantly lower, reflecting the first sphere’s blocking of the flow seen by the second sphere. The corresponding Strouhal numbers are  $St_1(C_d) = 0.020$  and  $St_2(C_d) = 0.327$  for the first sphere, and  $St_1(C_d) = 0.020$  and  $St_2(C_d) = 0.337$  for the second sphere. The Strouhal number for the second sphere is similar to that for the single sphere, indicating similarities in the vortex shedding in the far wake, visible also in Fig. 16. In contrast, the Strouhal number for the first sphere is strongly affected by the presence of the obstacle in its immediate wake.

#### 4 Concluding remarks

A study exploring behaviour of stratified flows past spheres have been conducted using a newly developed parallel option of the nonoscillatory forward-in-time scheme operating on flexible unstructured meshes and employing finite volume spatial discretisation. The study repeated well documented benchmarks for neutrally-stratified flows at  $Re = 200$  and  $300$ , allowing for validation of the proposed numerical approach. Additionally, for the stably stratified flows at  $Re = 200$ , earlier numerical and experimental studies provided further means for qualitative and quantitative validation of the NFT-FV model.

Our study of stably stratified flows at  $Re = 300$  provides further insights into stratified flows at moderate Reynolds numbers. Detailed documentation of numerical simulations and their analysis was supplemented with comparisons with experimental data when available. The presented results confirmed the general experimental characterisation for stratified flows past a single sphere, introduced in [23]. In particular, they showed that the overall flow patterns are dominated by stratification as the Froude number decreases. Although entirely different at high Froude numbers—where the flow at  $Re = 200$  reaches the steady state and at  $Re = 300$  results in a periodic hairpin vortex shedding—at  $1/Fr = 1.6$  both flows become planar and are in the lee-wave instability regime. In this regime, both flows reach steady state except for tiny recirculations in the lee indicating the lee-waves breaking. Differences between the two flows are in the details, such as the lengths of the recirculations formed behind a sphere that can be observed in the central horizontal plane. This similarity between the flow patterns continues at lower Froude numbers where the flows enter a two-dimensional vortex shedding regime in the horizontal, while remaining planar in the vertical, e.g. at  $1/Fr = 4$ . Details of the stably stratified flow features, such as amplitudes and length of gravity waves, slightly differ between the two Reynolds numbers. For  $Re = 200$ , we also document the triggering of a transition to the 2D vortex shedding regime at  $1/Fr = 2.25$ . The exact transition between the regimes is dictated by viscosity and occurs

at lower Froude number for lower Reynolds numbers.

In addition, the single sphere study was extended to akin simulations of flows past two spheres, facilitated in the framework of unstructured meshes. The results for the neutrally stratified flow at  $Re = 300$  are in good agreement with those reported in the literature [57] and further confirm the validity of the NFT-FV model. The stratified flow past two spheres is, to our knowledge, documented for the first time and investigated for the chosen tandem configuration at  $Re = 300$  with  $1/Fr = 1.6$  and  $1/Fr = 4$ . The resulting flow patterns generally follow that recorded for the single sphere, however, a detailed analysis reveals particularities of the spheres' interactions that can be quite complex. These interactions can be associated with intricacies of atmospheric/oceanic flows past mountain ranges, islands and complex bathymetry [21,34,56], since they depend on the relative placement of the two spheres [57]. The tandem sphere simulations illustrate the potential of the NFT-FV solver operating on flexible meshes to provide a further insight into the class of stratified flows pertinent to engineering and geophysics, suggesting interactions between multiple spheres. Our preliminary simulations indicate that, similarly as for neutrally stratified flows, the flow patterns for multiple spheres are sensitive to the distance between the spheres and their relative location with respect to the flow direction. Identification of the flow regimes for configurations of multiple spheres will be studied in our future work.

Regardless of the overall satisfactory outcome of the study, it remains puzzling why numerical results for flows past a single sphere depart from experimental measurements for strong stratifications with  $1/Fr > 5$ , Figs. 10 and 12. Furthermore, the results using two distinct numerical models—ours and that of [30], available for  $Re = 200$ —give drag coefficients that agree well with each other, Fig. 10. The numerical results using yet another model [12], available for  $1/Fr = 5$  and  $Re = 100$ , also appear to overestimate the drag coefficient. The design of numerical experiments is essentially the same for our and [30] calculations, where reduction of the Froude number is achieved by increasing the ambient stratification  $S$  (defined in §2.1). However in [12] the stratification is fixed, and the Froude number reduction is achieved by increasing the sphere's radius. The authors in [30] attribute the drag discrepancy to the loss of the resolution, which is plausible because as  $Fr \searrow 0$  the amplitude of the fluid parcel vertical displacements,  $\eta$ , scales as  $\eta = 0.5DFr$ , based on the dividing streamline arguments [51]. However, based on the same arguments, increasing the sphere radius effectively fixes the magnitude of the displacements and thus their effective resolution. Consequently, the result of [12] is at odds with the insufficient resolution hypothesis. Moreover, as the only common element in all three numerical designs is the Boussinesq approximation adopted in the governing equations, one might speculate invalidity of the Boussinesq model in the limit of small Froude numbers. Indeed, in our and [30] experiments the ratio of the parcel displacements and the density (or potential temperature)

height scale  $S^{-1}$  increases as  $Fr \searrow 0$ . Yet this ratio  $\eta S$  is fixed in [12], which is again at odds with such speculations. Running out of ideas on how to blame the numerical results, we turn to experimental data. The design of the laboratory experiments in [26] was special, in that the size of the sphere and the ambient stratification were fixed with the buoyancy frequency  $N \propto Re/Fr$  (cf. §5.2 in [51] for discussion), effectively associating the Froude number reduction with the threading (viz. free stream) velocity. In such a design  $Re \searrow 0$  as  $Fr \searrow 0$ , with  $C_d$  and  $\Delta C_d$  vanishing in the limit. On one hand, this shows an elementary incompatibility of these experimental data with the numerical experiments discussed, or vice versa. On the other hand it adds to the intricacy of the  $Fr \searrow 0$  limit, potentially rejuvenating interests in the asymptotic [8] theories.

*Acknowledgements:* This work was supported in part by the funding received from the EPSRC studentship grant 1965773, Horizon 2020 Research and Innovation Programme (ESIWACE Grant agreement no. 675191, ESCAPE Grant agreement no. 671627 and ESCAPE2 Grant agreement no. 800897). This publication reflects the views only of the authors, and the Commission cannot be held responsible for any use which may be made of the information contained therein. The computation in this paper used the 'Hydra' High Performance System at Loughborough University. NCAR is sponsored by the National Science Foundation.

## References

- [1] P. Bagchi, S. Balachandar, Steady planar straining flow past a rigid sphere at moderate Reynolds number, *J. Fluid Mech.* 466 (2002) 365–407.
- [2] K.A. Brucker, S. Sarkar, A comparative study of self-propelled and towed wakes in a stratified fluid, *J. Fluid Mech.* 652 (2010) 373–404.
- [3] J.M. Chomaz, P. Bonneton, E.J. Hopfinger, The structure of the near wake of a sphere moving horizontally in a stratified fluid, *J. Fluid Mech.* 254 (1993) 1–21.
- [4] G. Constantinescu, M. Chapelet, K. Squires, Turbulence modeling applied to flow over a sphere, *AIAA J.* 41 (2003) 1733–1742.
- [5] P.J. Diamessis, G.R. Spedding, J.A. Domaradzki, Similarity scaling and vorticity structure in high-Reynolds-number stably stratified turbulent wakes, *J. Fluid Mech.* 671 (2011) 52–95.
- [6] J.A. Domaradzki, Z. Xiao, P.K. Smolarkiewicz, Effective eddy viscosities in implicit large eddy simulations of turbulent flows, *Phys. Fluids* 15 (2003) 3890–3893.

- [7] D.G. Dommermuth, J.W. Rottman, G.E. Innis, E.A. Novikov, Numerical simulation of the wake of a towed sphere in a weakly stratified fluid, *J. Fluid Mech.* 473 (2002) 83–101.
- [8] P.G. Drazin, On the steady flow of a fluid of variable density past obstacle, *Tellus* 13 (1961) 239–251.
- [9] M. Esmailpour, J.E. Martin, P.M. Carrica, Near-field flow of submarines and ships advancing in a stable stratified fluid, *Ocean Eng.* 123 (2016) 75–95.
- [10] B. Fornberg, Steady viscous flow past a sphere at high Reynolds numbers, *J. Fluid Mech.* 190 (1988) 471–489.
- [11] M.J. Gourlay, S.C. Arendt, D.C. Fritts, J. Werne, Numerical modeling of initially turbulent wakes with net momentum, *Phys. Fluids* 13 (12) (2001) 3783–3802.
- [12] V.A. Gushchin and R.V. Matyushin, Vortex formation mechanisms in the wake behind a sphere for  $200 < Re < 380$ , *Fluid Dynamics*, 41 (2006) 795–809.
- [13] V.A. Gushchin, P.V. Matyushin, Simulation and study of stratified flows around finite bodies, *Comput. Math. Math. Phys.* 56 (6) (2016) 1034–1047.
- [14] H. Hanazaki, A numerical study of 3-dimensional stratified flow past a sphere, *J. Fluid Mech.* 192 (1988) 393–419.
- [15] H. Honji, Vortex motions in stratified wake flows, *Fluid Dyn. Res.* 3 (1988) 425–430.
- [16] J.C.R. Hunt, W.H. Snyder, Experiments on stably and neutrally stratified flow over a model 3-dimensional hill, *J. Fluid Mech.* 96 (1980) 671–704.
- [17] J. Jeong, F. Hussain, On the identification of a vortex, *J. Fluid Mech.* 285 (1995) 69–94.
- [18] T.A. Johnson, V.C. Patel, Flow past a sphere up to a Reynolds number of 300, *J. Fluid Mech.* 378 (1999) 19–70.
- [19] G. Karypis, V. Kumar, A fast and high quality multilevel scheme for partitioning irregular graphs, *SIAM J. Sci. Comput.* 20 (1) (1998) 359–392.
- [20] C. Kühnlein, W. Deconinck, R. Klein, S. Malardel, Z.P. Piotrowski, P.K. Smolarkiewicz, J. Szmelter, N.P. Wedi, FVM 1.0: a nonhydrostatic finite-volume dynamical core for the IFS, *Geosc. Model Dev.* 12 (2019) 651–676.
- [21] J.T. Lee, R.E. Lawson Jr., G.L. Marsh, Flow visualisation experiments on stably stratified flow over ridges and valleys, *Meteorol. Atmos. Phys.* 37 (1987) 183–194.
- [22] S. Lee and K.S. Yang, Flow past a sphere in density-stratified fluid, *Theoret. Comput. Fluid Dyn.* 18 (2004) 265–276.
- [23] Q. Lin, W.R. Lindberg, D.L. Boyer, H.J.S. Fernando, Stratified flow past a sphere, *J. Fluid Mech.* 240 (1992) 315–354.

- [24] F.B. Lipps, R.S. Hemler, A scale analysis of deep moist convection and some related numerical calculations, *J. Atmos. Sci.* 39 (1982) 2192–2210.
- [25] F.B. Lipps, On the anelastic approximation for deep convection, *J. Atmos. Sci.* 47 (1990) 1794–1798.
- [26] K.E.B. Lofquist, L.P. Purtell, Drag on a sphere moving horizontally through a stratified liquid, *J. Fluid Mech.* 148 (1984) 271–284.
- [27] L.G. Margolin, P.K. Smolarkiewicz, Z. Sorbjan, Large-eddy simulation of convective boundary layers using nonoscillatory differencing, *Physica D* 133 (1999) 390–397.
- [28] L.G. Margolin, P.K. Smolarkiewicz, A.A. Wyszogrodzki, Dissipation in implicit turbulence models: A computational study, *J. Appl. Mech. Tran. ASME* 73 (2006) 469–473.
- [29] I. Nakamura, Steady wake behind a sphere, *Phys. Fluids* 19 (1976) 5–8.
- [30] T.S. Orr, J.A. Domaradzki, G.R. Spedding, G.S. Constantinescu, Numerical simulations of the near wake of a sphere moving in a steady, horizontal motion through a linearly stratified fluid at  $Re=1000$ , *Phys. Fluids* 27 (2015) 035113.
- [31] A. Pal, S. Sarkar, A. Posa, E. Balaras, Regeneration of turbulent fluctuations in low-Froude-number flow over a sphere at a Reynolds number of 3700, *J. Fluid Mech.* 804 (2016) R2.
- [32] A. Pal, S. Sarkar, A. Posa, E. Balaras, Direct numerical simulation of stratified flow past a sphere at a subcritical Reynolds number of 3700 and moderate Froude number, *J. Fluid Mech.* 826 (2017) 5–31.
- [33] J.M. Prusa, P.K. Smolarkiewicz, A.A. Wyszogrodzki, EULAG, a computational model for multiscale flows, *Comput. Fluids* 37 (2008) 1193–1207.
- [34] J.M. Reisner, P.K. Smolarkiewicz, Thermally forced low Froude-number flow past 3-dimensional obstacles, *J. Atmos. Sci.* 51 (1994) 117–133.
- [35] R.B. Smith, Linear theory of stratified hydrostatic flow past an isolated mountain, *Tellus* 32 (1980) 348–364.
- [36] R.B. Smith, Linear theory of hydrostatic flow over an isolated mountain in isosteric coordinates, *J. Atmos. Sci.* 45 (1988) 3889–3896.
- [37] P.K. Smolarkiewicz, R. Rotunno, Low Froude number flow past three-dimensional obstacles. Part I: Baroclinically generated lee vortices, *J. Atmos. Sci.* 46 (1989) 1154–1164.
- [38] P.K. Smolarkiewicz, L.G. Margolin, On forward-in-time differencing for fluids: Extension to a curvilinear framework, *Month. Weather Rev.* 121 (1993) 1847–1859.
- [39] P.K. Smolarkiewicz, V. Grubišić, L.G. Margolin, On forward-in-time differencing for fluids: stopping criteria for iterative solutions of anelastic pressure equations, *Month. Weather Rev.* 125 (1997) 647–654.

- [40] P.K. Smolarkiewicz, J. Szmelter, Multidimensional positive definite advection transport algorithm (MPDATA): an edge-based unstructured-data formulation, *Int. J. Numer. Methods Fluids* 47 (2005) 1293–1299.
- [41] P.K. Smolarkiewicz, J. Szmelter, MPDATA: an edge-based unstructured-grid formulation, *J. Comput. Phys.* 206 (2005) 624–649.
- [42] P.K. Smolarkiewicz, J. Szmelter, Iterated upwind schemes for gas dynamics, *J. Comput. Phys.* 228 (2009) 33–54.
- [43] P.K. Smolarkiewicz, J. Szmelter, A nonhydrostatic unstructured-mesh soundproof model for simulation of internal gravity waves, *Acta Geophys.* 59 (2011) 1109–1134.
- [44] P.K. Smolarkiewicz, J. Szmelter, A.A. Wyszogrodzki, An unstructured-mesh atmospheric model for nonhydrostatic dynamics, *J. Comput. Phys.* 254 (2013) 184–199.
- [45] P.K. Smolarkiewicz, W. Deconinck, M. Hamrud, C. Kühnlein, G. Mozdzyński, J. Szmelter, N.P. Wedi, A finite-volume module for simulating global all-scale atmospheric flows, *J. Comput. Phys.* 315 (2016) 287–304.
- [46] P.K. Smolarkiewicz, J. Szmelter, F. Xiao, Simulation of all-scale atmospheric dynamics on unstructured meshes, *J. Comput. Phys.* 322 (2016) 267–287.
- [47] P.K. Smolarkiewicz, C. Kühnlein, N.P. Wedi, Semi-implicit integrations of perturbation equations for all-scale atmospheric dynamics, *J. Comput. Phys.* 376 (2019) 145–159.
- [48] J. Szmelter, M.J. Marchant, A. Evans, N.P. Weatherill, 2-Dimensional Navier-Stokes equations with adaptivity on structured meshes, *Comput. Meth. Applied Mech. and Eng.*, 101 (1992) 355–368.
- [49] J. Szmelter, P.K. Smolarkiewicz, An edge-based unstructured mesh framework for atmospheric flows, *Comput. Fluids*. 46 (2011) 455–460.
- [50] J. Szmelter, Z. Zhang, P.K. Smolarkiewicz, An unstructured-mesh atmospheric model for nonhydrostatic dynamics: towards optimal mesh resolution, *J. Comput. Phys.* 294 (2015) 363–381.
- [51] J. Szmelter, P.K. Smolarkiewicz, Z. Zhang, Z.X. Cao, Non-oscillatory forward-in-time integrators for viscous incompressible flows past a sphere, *J. Comput. Phys.* 386 (2019) 365–383.
- [52] S. Taneda, Experimental investigation of the wake behind a sphere at low Reynolds numbers, *J. Phys. Soc. Japan*, 11 (1956) 1104–1108.
- [53] A.G. Tomboulides, S.A. Orszag, Numerical investigation of transitional and weak turbulent flow past a sphere, *J. Fluid Mech.* 416 (2000) 45–73.
- [54] A. VanDine, K. Chongsiripinyo, S. Sarkar, Hybrid spatially-evolving DNS model of flow past a sphere, *Comput. Fluids* 171 (2018) 41–52.

- [55] S.B. Vosper, Three-dimensional numerical simulations of strongly stratified flow past conical orography, *J. Atmos. Sci.* 57 (2000) 3716–3739.
- [56] A. Warn-Varnas, J. Hawkins, P.K. Smolarkiewicz, S.A. Chin-Bing, D. King, Z. Hallock, Solitary wave effects north of Strait of Messina, *Ocean Modelling* 18 (2007) 97–121.
- [57] D.H. Yoon, K.S. Yang, Characterization of flow pattern past two spheres in proximity, *Phys. Fluids* 21 (2009) 073603.